Supplementary Material

This document contains the supplementary tables and figures accompanying the main manuscript. The following additional files are provided through the EEET platform under the Supplementary Online Material section: Field_data.xlsx (field data), carbon_vulnerability_pipeline.R (main analysis script), console_R_output_Model.txt (R model console output), Dataset_model.csv (model dataset), LandTrendr_plot_metrics.csv (per-plot LandTrendr metrics), LandTrendr_GEE_code.js (Google Earth Engine code for LandTrendr), collinearity_R.R (collinearity analysis script), and console_R_collinearity.txt (collinearity analysis console output).

Supplementary Tables

Table S1. Detailed validation statistics of the volume tables provided by the Moroccan Agence Nationale des Eaux et Forêts (ANEF) and used to estimate standing timber volume in this study. Statistics apply only to the five species with a local volume table; the three Juniperus species are estimated through direct allometric equations (see Table 2 in the main manuscript).

Species	Equation (V in dm³)	R^2	σ_e	σ_r	Bias $\bar{e}$ (%)	N (trees)	C range (cm)	DBH range (cm)
Quercus rotundifolia	$V = -77.469 + 2.918 \cdot C + 0.002 \cdot C^2$	0.981	2.63	34.6	1.4	87	21–188	7–60
Pinus halepensis	$V = -122.033 + 5.217 \cdot C - 0.253 \cdot H \cdot C + 0.002 \cdot H \cdot C^2$	0.950	30.31	55.5	1.76	56	26–172	8–55
Pinus pinaster	$V = 0.075 + 0.097 \cdot H \cdot C + 0.038 \cdot H \cdot C^2$	0.985	5.74	14.5	2.3	35	26–114	8–36
Tetraclinis articulata	$V = -10.263 + 0.465 \cdot C + 0.013 \cdot C^2$	0.911	0.282	3.39	0.16	86	22–72	7–23
Cupressus arizonica	$V = 21.103 + 0.003 \cdot H \cdot C^2$	0.983	7.86	11.9	4.9	100	20–90	6–29

Note: V = standing timber volume (dm³); C = circumference at breast height (1.30 m, cm); H = total tree height (m); H·C = product of H and C; σ_e = standard error of estimate (dm³); σ_r = residual standard deviation (dm³); $\bar{e}$ = mean relative bias of predicted versus observed volume (%); N = calibration sample size; DBH range computed as C/π and rounded to the nearest cm.

Table S2. Stratum-wise decomposition of the 2×2 confusion matrix between spectral detection (disturb_bin, prop_change > 0.5 in 3×3 buffer) and field observation of mortality ≥ 15% of stems DBH ≥ 6 cm (disturb_field). Sensitivity, Specificity and OA indicators are reported by stratum. The aggregated overall table is reported in the main manuscript (Table 8). Methodology following Olofsson et al. (2014).

Stratum	n	TP	FP	FN	TN	Field obs.	Spectral pred.	OA	Sens.	Spec.
S1 (Open–cool)	18	10	3	0	5	0.556	0.722	0.833	1.000	0.625

Stratum	n	TP	FP	FN	TN	Field obs.	Spectral pred.	OA	Sens.	Spec.
S2 (Open–warm)	17	11	2	0	4	0.647	0.765	0.882	1.000	0.667
S3 (Moderate–cool)	4	3	1	0	0	0.750	1.000	0.750	1.000	n.d.
S4 (Moderate–warm)	11	7	3	0	1	0.636	0.909	0.727	1.000	0.250
S5 (Dense–cool)	5	3	1	0	1	0.600	0.800	0.800	1.000	0.500
S6 (Dense–warm)	5	3	2	0	0	0.600	1.000	0.600	1.000	n.d.
Total	**60**	**37**	**12**	**0**	**11**	**0.617**	**0.817**	**0.800**	**1.000**	**0.478**

Note. Sensitivity = 1.000 in all strata: no field mortality is missed by spectral detection. Specificity varies from 0.250 (S4) to 0.667 (S2), with n.d. for S3 and S6 (TN = 0 or insufficient n). FP = 12, FN = 0, McNemar exact p = 0.0005 (overall test). This controlled over-detection of partial dieback is consistent with the early spectral signature of "non-catastrophic" disturbances (Cohen et al., 2018; Wulder et al., 2019). See §3.3 of the main manuscript.

Table S3. Operational parameters and validation metrics of the stratification protocol. Section A documents the Random Forest classification of canopy density on Sentinel-2 imagery; Section B documents the Heat Load Index dichotomization. Class areas and plot allocations per stratum are reported in Table 1 of the main manuscript.

Element	Specification
A. Canopy density — Random Forest classification	
Platform	Google Earth Engine (ee.Classifier.smileRandomForest)
Input imagery	Sentinel-2 Level-2A, May–September 2025 composite
Predictors (6)	B2, B3, B4, B8 (surface reflectance); NDVI; NDMI
Variable importance (Gini-impurity, decreasing)	B4 ≈ 2 000 > NDVI ≈ 1 750 > NDMI ≈ 1 450 > B2 ≈ 1 100 > B8 ≈ 1 050 > B3 ≈ 850
Training sample size	19 517 pixels
Class distribution (training)	Non-forest: 5 000 / Open: 5 000 / Moderate: 5 000 / Dense: 4 517
Hyperparameters	GEE defaults of ee.Classifier.smileRandomForest
Overall accuracy (test)	0.813
Cohen's κ (test)	0.751
F1 macro (test)	0.814
Operational thresholds	Open: canopy cover < 30 %; Moderate: 30–60 %; Dense: > 60 %
B. Thermal exposure — Heat Load Index (HLI)	
Source	McCune and Keon (2002)

Element	Specification
Input DEM	SRTM, 30 m
Observed HLI range (forest mask)	0.17 – 1.00
Dichotomization threshold	0.74 (median of HLI distribution over the forest mask)
Classes	Cool: HLI < 0.74; Warm: HLI ≥ 0.74

Note: The Non-forest class is used to derive the forest mask only. The three forest classes (Open / Moderate / Dense), crossed with the two HLI classes (Cool / Warm), yield the six strata S1–S6 of the study (Table 1 of the main manuscript). The variable importance values are read from Supplementary Figure S2.

Supplementary Figures

Figure S1. Canopy density classification of the study area derived from a Random Forest classifier applied to a Sentinel-2 Level-2A May–September 2025 composite (six predictors: B2, B3, B4, B8, NDVI, NDMI; 19,517 training pixels; overall accuracy = 0.813; κ = 0.751; F1 macro = 0.814; Supplementary Table S3). Four classes are mapped: Non-forest (red), Low (canopy cover < 30 %), Medium (30–60 %) and High (> 60 %), shown along a graduated green palette. The Non-forest class is used to derive the forest mask only; the three forest classes (Low / Medium / High), crossed with the two HLI classes (Figure S3), yield the six strata S1–S6 of the study. Coordinate system: WGS84.

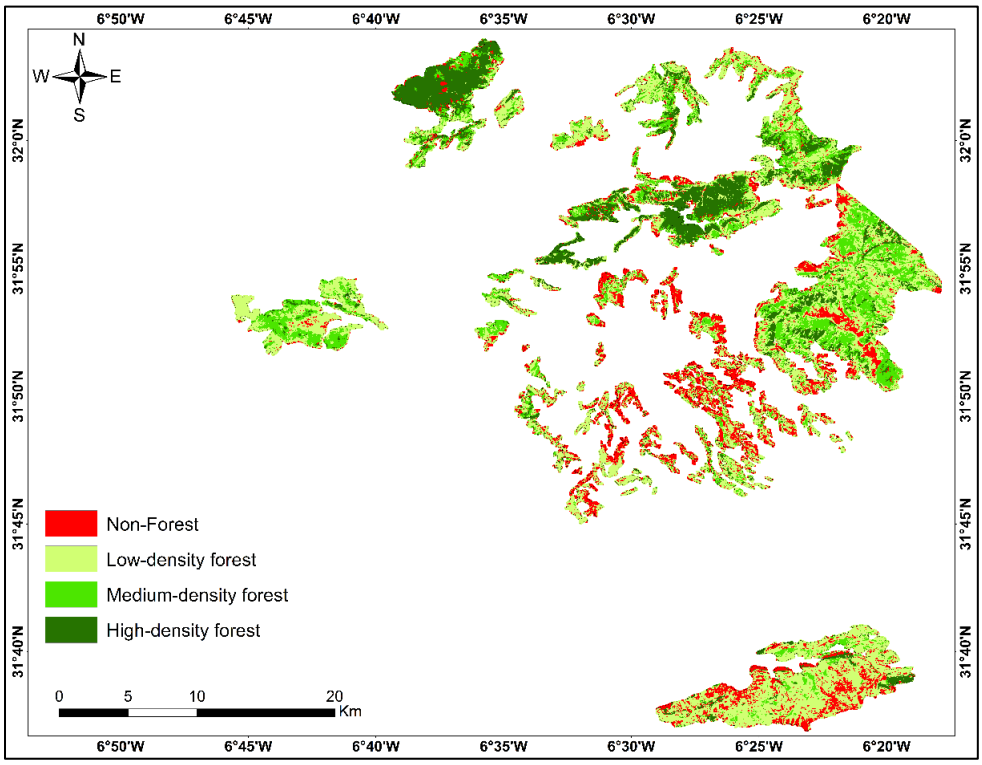

Figure S2. Random Forest variable importance for the canopy density classification on Sentinel-2 imagery (May–September 2025 composite). Importance is reported as the Gini impurity decrease summed across all trees of the forest. The six predictors used were the surface reflectance bands B2, B3, B4, B8 and two derived indices (NDVI, NDMI). Red band B4 and NDVI contribute the most to class separability, followed by NDMI; the visible bands B2 and B3 carry the lowest contribution.

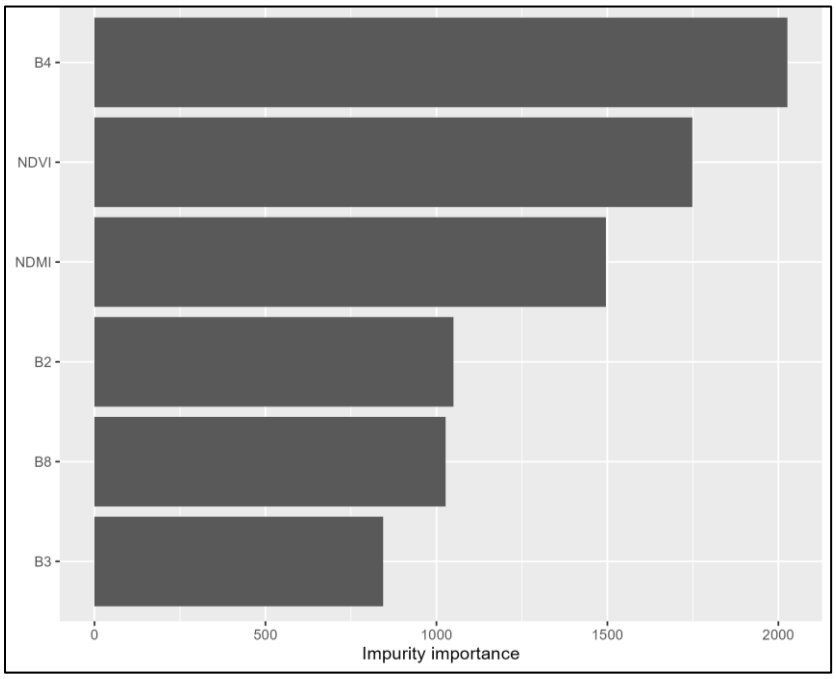

Figure S3. Spatial distribution of the Heat Load Index (HLI; McCune and Keon, 2002) over the forest mask. HLI was computed at 30 m resolution from the SRTM digital elevation model and integrates slope, aspect and latitude into a topographic proxy of incoming radiation load. Observed values range from 0.17 (coolest slopes, green) to 1.00 (warmest slopes, red); the median value of 0.74 was used as the dichotomization threshold between the Cool (HLI < 0.74) and Warm (HLI ≥ 0.74) classes used in the stratification (Supplementary Table S3). Coordinate system: WGS84.

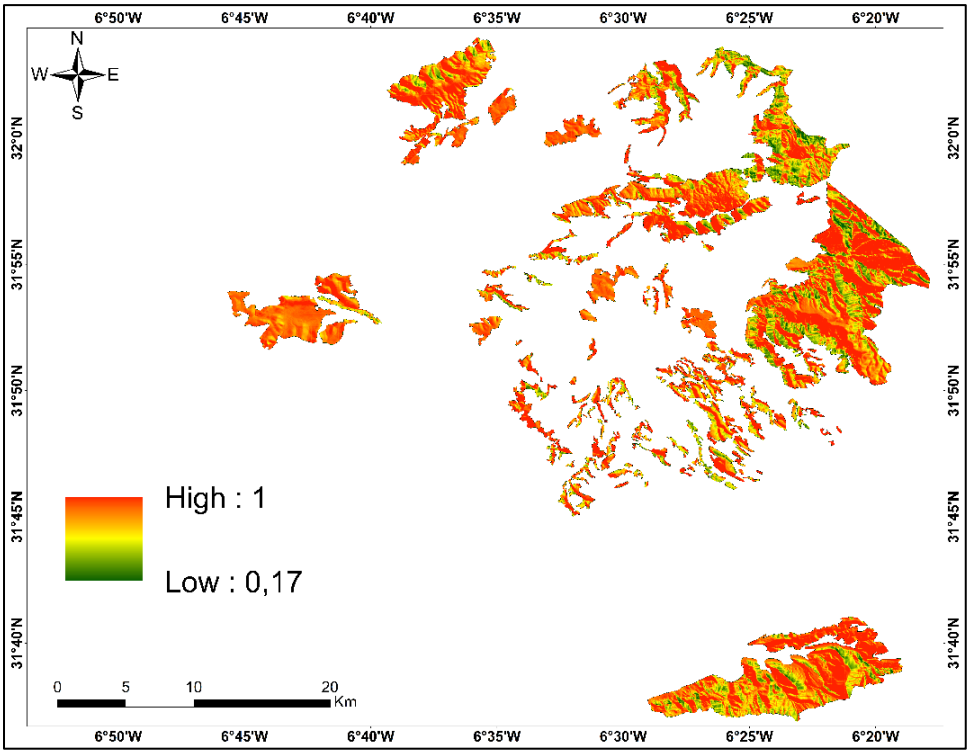

Figure S4. Final stratification of the study area into the six strata S1–S6 used in the analyses. The six strata result from crossing the three canopy density classes (Low, Medium, High) with the two thermal exposure classes (Cool, Warm; Supplementary Figure S3). Stratum labels: S1 = Low-density × Cool, S2 = Low-density × Warm, S3 = Medium-density × Cool, S4 = Medium-density × Warm, S5 = High-density × Cool, S6 = High-density × Warm. Stratum areas, percentage coverage and plot allocations are reported in Table 1 of the main manuscript. Coordinate system: WGS84.

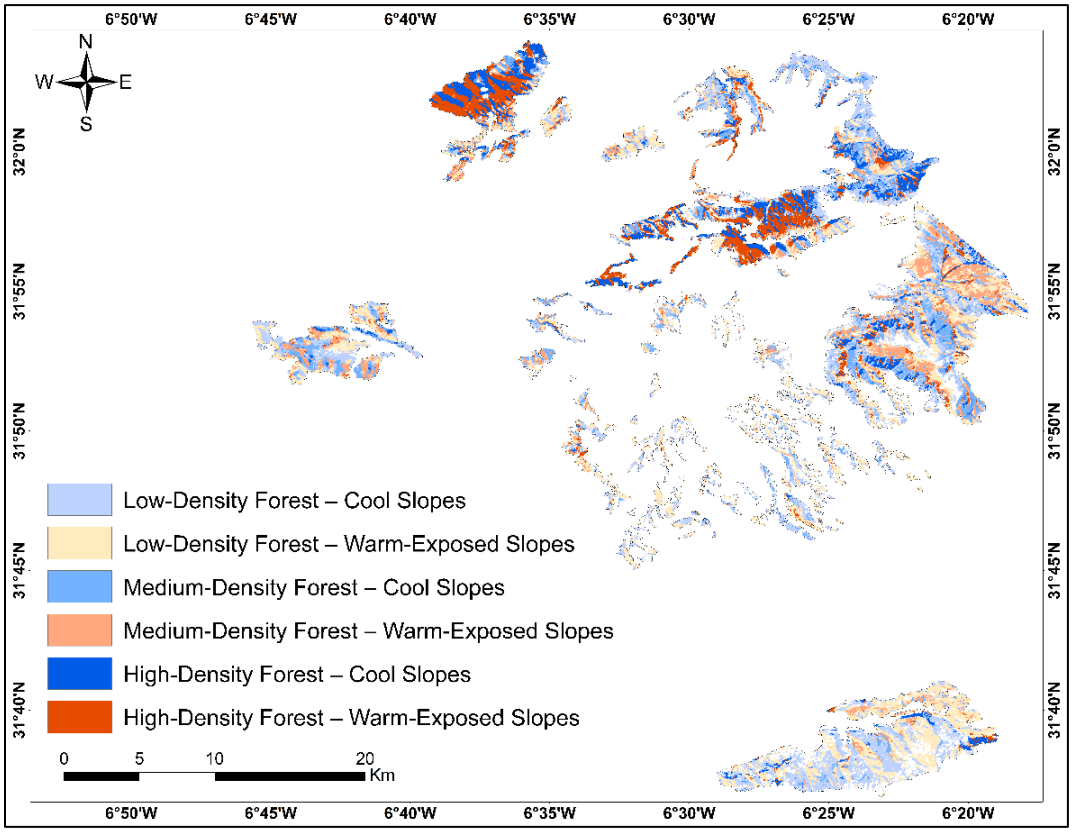

Figure S5. Field photographic examples of the four tree health classes used in the inventory protocol. (A) Live trees with no visible defoliation or dieback symptoms; (B) Lightly declining trees with moderate symptoms (partially dry foliage, limited defoliation, small dead branches) affecting less than approximately 30 % of the crown; (C) Severely declining trees with declining symptoms (dead branches, marked defoliation, strongly reduced crown) dominating more than approximately 50 % of the crown, with a living portion still visible; (D) Standing dead trees with no living foliage. Mortality signs on the trunk affecting approximately 15 % or more of the circumference were also recorded and denoted local cambium alteration or advanced degradation. Photographs taken during the 2025 field campaign in the Azilal Province forest district.

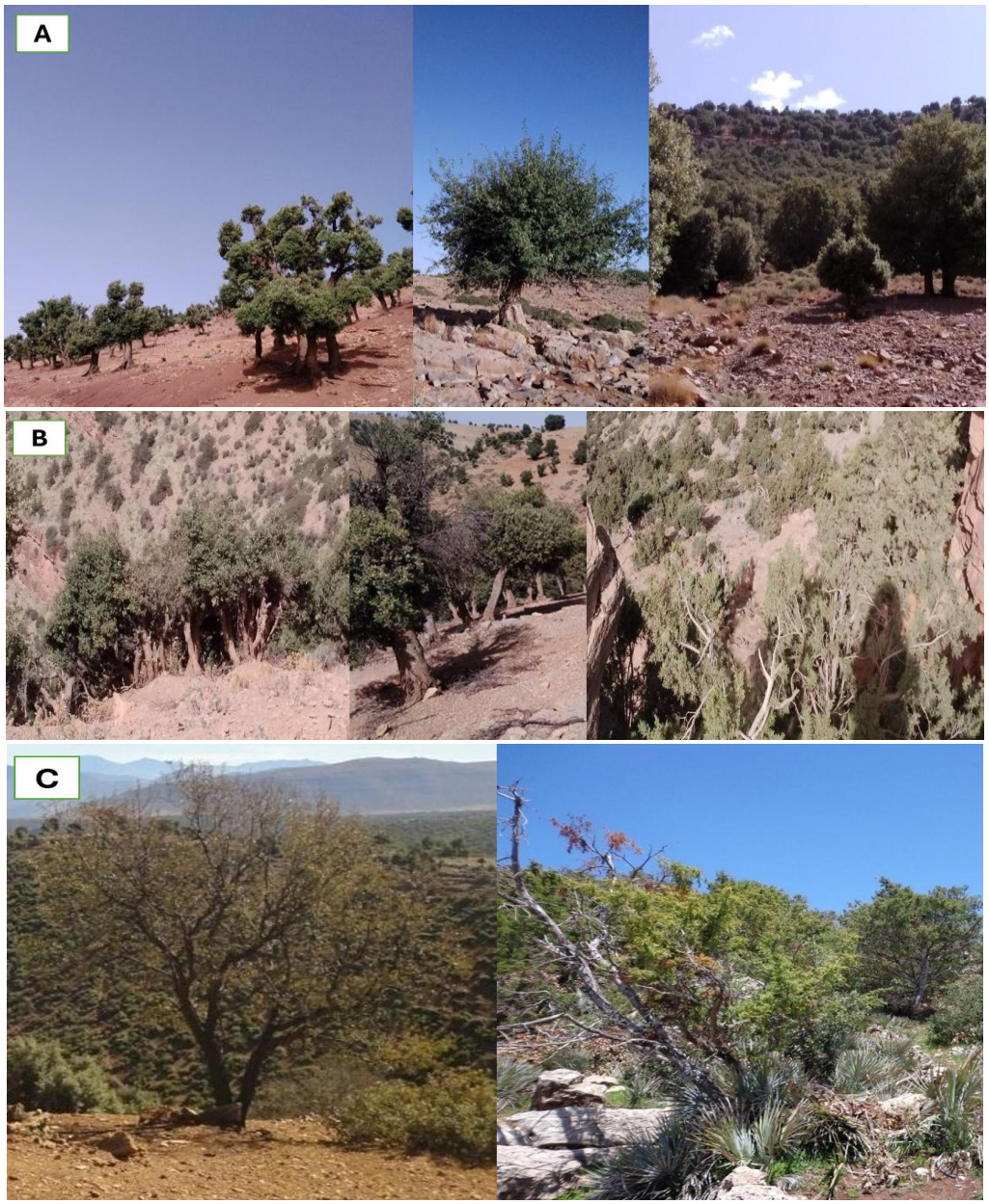

Figure S6. Examples of LandTrendr-detected spectral trajectories for six representative plots of the inventory, illustrating the diversity of disturbance signals captured by the segmentation algorithm. For each plot, the annual NBR time series (1995–2025) is shown together with the LandTrendr-fitted segments (vertical markers indicate detected breakpoints). The six examples span the gradient from gradual to abrupt disturbances and from low- to high-magnitude events. The fitted segments are used downstream to derive the per-plot disturbance probability (disturb_bin), magnitude (ΔNBR × 1,000) and recovery score ($\hat{R}$) that enter the composite vulnerability index defined in the main manuscript.

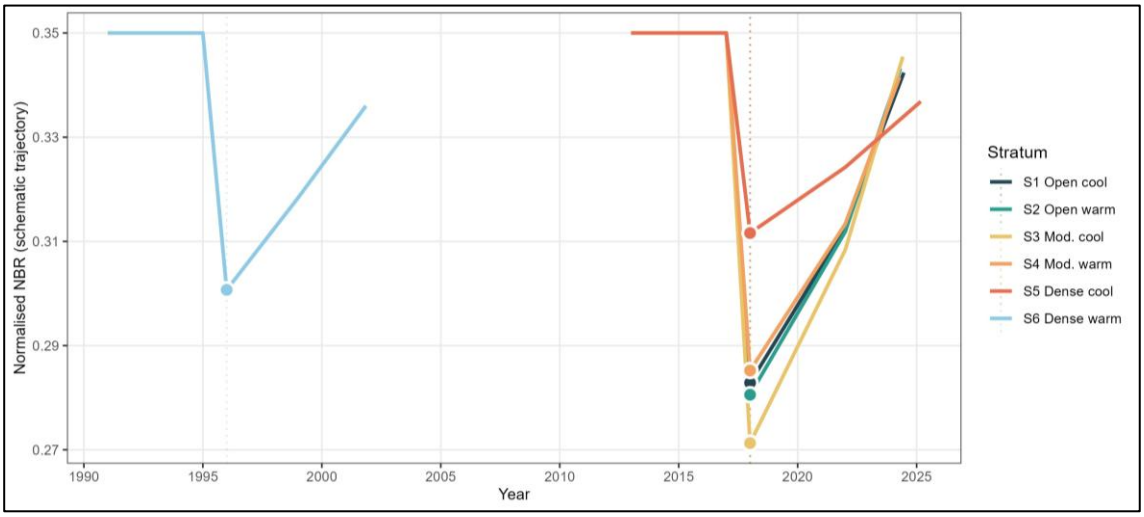

Figure S7. Out-of-sample performance comparison of the three candidate logistic regression models for the probability of spectral disturbance at the plot level: V2 (unpenalized standard maximum likelihood; predictors: Elev, HLI, SPEI-12), V5 (Firth-penalized; same predictors as V2) and V6-B (Firth-penalized; predictors: WC_Pseas_CV, HLI, SPEI-12). The bars report the leave-one-out cross-validation AUC (LOO-CV AUC) and the Riley shrinkage factor (η) for each model. V6-B reaches the highest LOO-CV AUC (0.733) and an η of 0.886 approaching the conservative 0.90 threshold (Riley et al., 2019; van Smeden et al., 2019); V5 reaches 0.649 in AUC; V2 falls to 0.645 in AUC despite a high apparent shrinkage of 0.984, a discrepancy that motivates its exclusion from the main inference. V6-B was retained as the main model; V5 was kept as a sensitivity analysis.

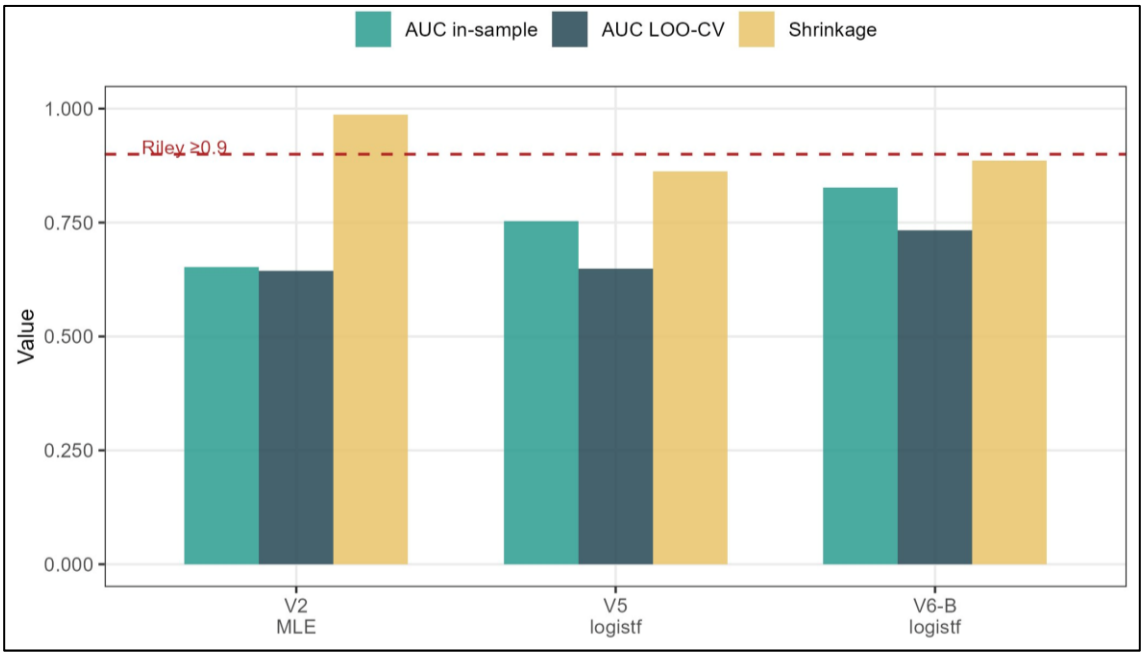

Figure S8. Statistical diagnostics of the main logistic regression model V6-B (Firth-penalized; predictors: precipitation seasonality WC_Pseas_CV, Heat Load Index HLI, minimum 12-month SPEI; n = 52 plots). (A) Standardized Pearson residuals plotted against the fitted disturbance probabilities; (B) Cook's distance per observation flagging high-leverage plots; (C) calibration plot comparing observed and predicted probabilities by deciles; (D) receiver operating characteristic (ROC) curve with LOO-CV AUC = 0.733. The diagnostics confirm the absence of marked residual heteroscedasticity and of residual collinearity once elevation was dropped (all VIF < 1.2 within V6-B). Riley shrinkage = 0.886.

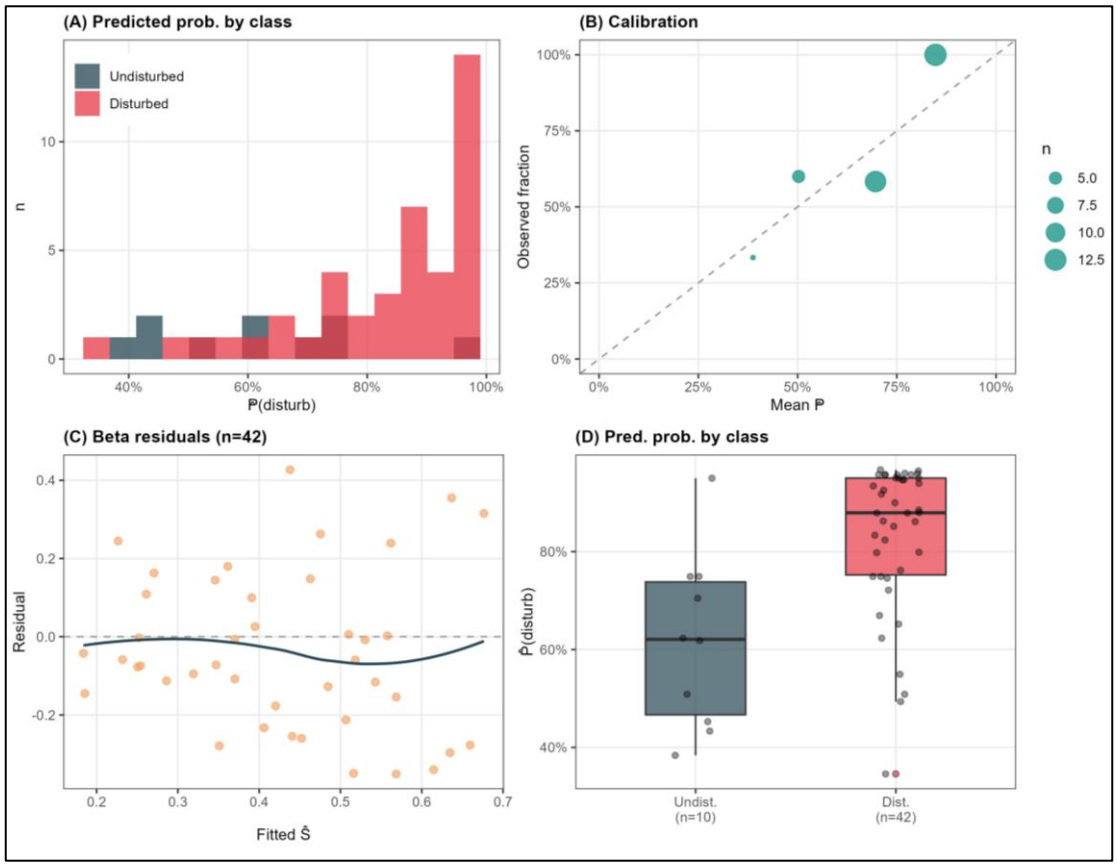

Figure S9. Statistical diagnostics of the sensitivity-analysis model V5 (Firth-penalized; predictors: elevation, Heat Load Index HLI, minimum 12-month SPEI; n = 52 plots). The four panels mirror those of Figure S8 for V6-B: (A) standardized Pearson residuals against fitted probabilities, (B) Cook's distance per observation, (C) calibration plot, and (D) ROC curve (LOO-CV AUC = 0.649). V5 was retained as a sensitivity analysis after V6-B was selected as the main model: V6-B exceeded V5 by 8.4 points in LOO-CV AUC, and its Riley shrinkage (0.886) was closer to the conservative 0.90 threshold than that of V5. Comparison with Figure S8 documents the robustness of the climatic signal across the two competing variable specifications.

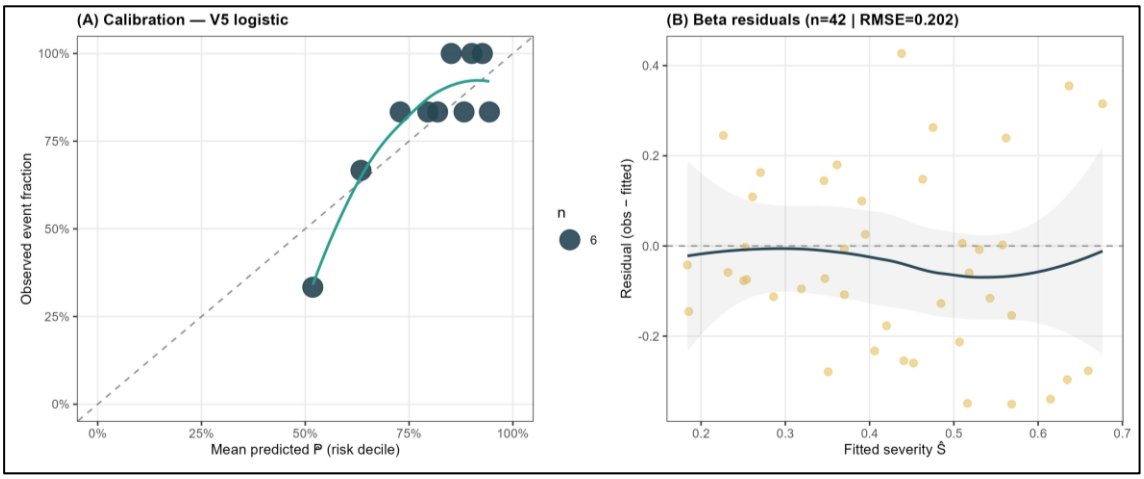

Figure S10. Monte Carlo distribution of total stand aboveground biomass under joint perturbation of ρ and BEF. For each species, ρ and BEF were independently multiplied by random factors drawn from normal distributions N(1, σ_ρ²) and N(1, σ_BEF²), with σ_ρ = 0.10 and σ_BEF = 0.15. The histogram shows the resulting distribution of total stand AGB (t). The distribution is approximately symmetric and centered on a median of 260.4 kt, with a 90 % empirical interval [P5; P95] = [193.7; 334.3] kt (mean 260.0 kt; n = 10,000 iterations). This figure quantifies the methodological uncertainty associated with the choice of conversion parameters (cf. §4 of the manuscript and Limitations section).

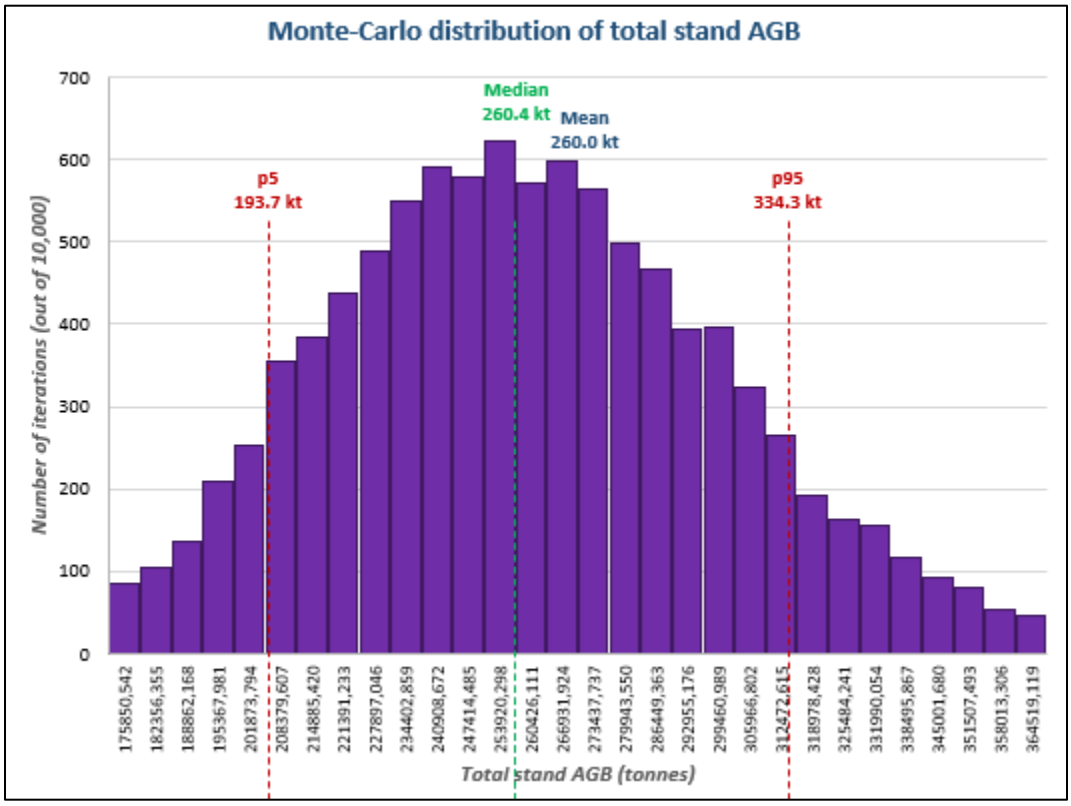

Figure S11. Collinearity diagnostics underlying the variable selection of the main logistic regression model V6-B. Top row (panels A–C): Pearson correlation matrices for (A) the three predictors of the V5 sensitivity-analysis model (Elev, HLI, SPEI; n = 60), (B) the three predictors of the main V6-B model (Pseas, SPEI, HLI; n = 52), and (C) the four-predictor diagnostic block jointly retaining Elev, HLI, SPEI and Pseas (n = 52). Pearson coefficients are colour-coded from blue (r = −1) to red (r = +1). Middle row (panels D–F): variance inflation factors (VIF) for the same three blocks, with dashed and dotted vertical lines marking the conservative (VIF = 5) and strict (VIF = 10) exclusion thresholds (Hair et al., 2014). Within V5 and V6-B taken separately (panels D and E), all VIFs remain below 1.2, confirming the absence of residual collinearity. Within the four-predictor block (panel F), both Elev and Pseas exceed the strict threshold (VIF = 12.13 and 12.10 respectively), reflecting their strong near-collinearity. Bottom row (panel G): bivariate scatter of precipitation seasonality (Pseas_CV, BIO15 WorldClim) against elevation (m) over the 52 plots with complete pre-disturbance climatic coverage; the red line shows the linear fit and its 95 % confidence band (Pearson r = −0.958; p < 0.001; n = 52). This diagnostic motivates the substitution of elevation by precipitation seasonality in model V6-B, with precipitation seasonality retained as the climatically interpretable surrogate of elevation in the High Atlas context.